J. Fluid Mech. (2023), *vol*. 977, A2, doi:10.1017/jfm.2023.931

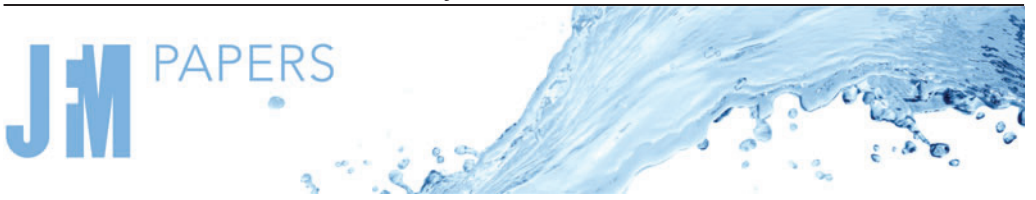

Gravity-coupled flutter and contact of a flag near a wall

Minseop Lee[1], Cheolgyun Jung[1], Jeongsu Lee[2] and Daegyoum Kim[1,†]

[1]Department of Mechanical Engineering, KAIST, Daejeon 34141, Republic of Korea

[2]Department of Mechanical, Smart and Industrial Engineering, Gachon University, Seongnam 13120, Republic of Korea

(Received 25 April 2023; revised 23 September 2023; accepted 30 October 2023)

The stability and postcritical behaviour of a horizontal flag undergoing gravity-induced deformation and periodic contact with a nearby horizontal rigid wall are experimentally investigated. The results elucidate the combined effects of gravity and contact on flutter, and reveal design principles for application to triboelectric energy harvesting. By varying the free-stream velocity, flag thickness and distance between the flagpole and the wall, the dynamics of the flag are classified into quasistatic equilibrium, flutter, partial contact and saturated contact modes. Considering the significance of gravitational effects, a new dimensionless flow velocity is proposed to identify the distribution of the dynamic modes, and its definition varies according to whether the wall is placed above or below the flag. The critical conditions for transitions between the dynamic modes are determined from the balance of fluid dynamic and gravitational effects. The distance from the flagpole to the wall is found to be more critical for transitions in the lower-wall configuration than in the upper-wall configuration. The peak contact force as well as the oscillation amplitude and frequency at postequilibrium exhibits remarkably different trends depending on the location of the wall. The peak contact force imposed on the wall by the fluttering flag weakens as the distance to the wall increases in the case of an upper wall, whereas it becomes stronger in the case of a lower wall.

Key words: flow-structure interactions

1. Introduction

The interaction of thin elastic sheets with a uniform flow has long been studied to understand biological phenomena such as leaves fluttering in the wind, snoring, animal

† Email address for correspondence: daegyoum@kaist.ac.kr

locomotion (e.g. Ellis, Williams & Shneerson 1993; Ristroph & Zhang 2008; Ryu *et al.* 2019; Zhang, Huang & Lu 2020; Yang *et al.* 2021) and industrial phenomena such as the production of papers or films and flow control devices for convective heat transfer (e.g. Watanabe *et al.* 2002; Shoele & Mittal 2014; Park *et al.* 2016; Lee *et al.* 2017; Jeong *et al.* 2022). A flag, which is considered to be an elastic sheet with a fixed front end and a free rear end, exhibits distinct behaviours depending on the flow conditions and material properties, ranging from a stable equilibrium state to an unstable postcritical state. Numerous studies on the critical conditions and dynamic characteristics of a flag subjected to a free stream parallel to the flag have been conducted, including experiments (Huang 1995; Zhang *et al.* 2000; Kumar, Arekar & Poddar 2021), high-fidelity numerical simulations (Farnell, David & Barton 2004*a*; Connell & Yue 2007; Huang, Shin & Sung 2007; Sawada & Hisada 2007; Wang & Tian 2019) and low-order theoretical modelling (Guo & Païdoussis 2000; Argentina & Mahadevan 2005; Alben & Shelley 2008; Eloy *et al.* 2008; Michelin, Smith & Glover 2008). In addition, the dynamics of a flag interacting with a nearby structure have been examined using a system of multiple flags (Zhu & Peskin 2003; Farnell, David & Barton 2004*b*; Jia *et al.* 2007; Ristroph & Zhang 2008; Schouveiler & Eloy 2009; Kim, Huang & Sung 2010; Tian *et al.* 2011; Mougel, Doaré & Michelin 2016) and a single flag considering the ground effect or an upstream bluff body (Akaydın, Elvin & Andreopoulos 2010; Dessi & Mazzocconi 2015; Kim, Kang & Kim 2017). A wall located close to a flag has also been considered, in which a considerable distance between the flag and the wall exists, precluding direct contact between them during the flutter of the flag. The presence of the nearby wall affects both the critical velocity and postcritical dynamics of the flag when the wall distance changes by several orders of magnitude (Alben 2015; Mougel & Michelin 2020) and serves a function similar to that of an added mass (Jaiman, Parmar & Gurugubelli 2014).

Regarding engineering applications, the flow-induced flutter of a flag has been used to convert fluid kinetic energy to electrical energy by implementing piezoelectric patches (Allen & Smits 2001; Taylor *et al.* 2001; Dunnmon *et al.* 2011; Giacomello & Porfiri 2011; Akcabay & Young 2012; Michelin & Doaré 2013; Lee *et al.* 2015). In the past decade, triboelectric nanogenerators (TENG) based on the direct contact–separation process of a fluttering flag with a rigid wall have also been proposed (Fan, Tian & Wang 2012; Bae *et al.* 2014; Quan *et al.* 2016; Zhao *et al.* 2016; Xu *et al.* 2017; Sun *et al.* 2020; Zhao *et al.* 2022). These studies have focused on evaluating the energy harvesting performance of TENG devices, rather than analysing the contact dynamics of a fluttering flag from the perspective of fluid–structure interactions. Recently, Lee, Kim & Kim (2021) experimentally investigated the behaviours of a fluttering flag that periodically collides with a rigid wall. As the dimensionless flow velocity increases, the flag shows diverse modes, sequentially transitioning from tapping to regular clapping to weakly chaotic and finally fully chaotic motions. Despite the interaction of the flag with the wall, the critical conditions for flutter and dynamic characteristics such as the amplitude and Strouhal number are barely affected by the presence of contact. By adopting a vertical configuration for the initial flag state and the wall, the model of Lee *et al.* (2021) indicates that the effect of gravity is less important than the effects of fluid inertia and flag bending.

Most preceding studies of flag flutter have neglected gravitational effects. Experimentally, the effect of gravity has been minimized by positioning a flagpole vertically and fabricating a flag from a sufficiently stiff material, which prevents three-dimensional deformation by sagging and twisting. Numerical simulations have generally excluded the gravitational term from the equation of flag motion, even for three-dimensional flag models (Yu, Wang & Shao 2012; Banerjee, Connell & Yue 2015; Tang & Lu 2015; Chen *et al.* 2020). However, to consider the more realistic situations

that occur in nature and to improve the performance of engineering applications, the flag behaviours should be comprehensively examined under gravity, because gravity dramatically changes the response of a flag subjected to a uniform flow. Using numerical simulations of a three-dimensional flag with a vertical flagpole, Huang & Sung (2010) found that the asymmetric initial configuration of a flag in the presence of gravity significantly influences the stability and flutter dynamics of the flag. Depending on the Froude number $Fr = gL/U^2$, based on the flag length L and free-stream velocity U, gravity has dual effects on flag stability. If the Froude number exceeds a certain level, the flag sags entirely and does not exhibit regular flutter because the strong gravitational force contributes to the stabilization of the flag. However, at small Froude numbers, the magnitude of the pressure force acting on the flag increases compared with the case under the same flow conditions without gravity, leading to a large oscillation amplitude. Furthermore, Hœpffner & Naka (2011) identified the generation of an oblique wave on the flag, which is attributable to the influence of gravity during the elevation of the flag by fluid force.

In this study, we experimentally investigate the behaviours of a flag under the influence of gravity and contact with a wall to unravel the fluid-dynamical principles of flutter-driven TENG devices. In contrast to most previous studies in which a flagpole is placed vertically, the flagpole is placed horizontally so that the flag is deflected downwards even in the absence of flow, as shown in figure 1(*a*). Furthermore, the flutter induced by a free stream may cause the flag to contact with a horizontal wall positioned above or below the flag. Our experimental models and measurement techniques are described in § 2. The behaviours of the flag are classified based on the contact process with the wall by varying free-stream velocity, wall distance and flag thickness in § 3.1. In § 3.2, new dimensionless parameters are proposed to characterize the fluid–structure interaction of our model, and the boundaries of mode transition are predicted from scaling analysis. The contact force and dynamics of a flag in the postequilibrium state accompanying periodic contacts are discussed in § 3.3. Finally, the key findings from this study are summarized in § 4.

2. Experimental set-up

Experiments were conducted in an open-loop wind tunnel. The wind tunnel had a cross-section of 60 cm × 60 cm and could produce a free-stream velocity U from 1.8–13.0 m s^{-1}. A flagpole, which clamped the leading edge of the flag, and a rigid wall were placed horizontally (figure 1*a*). Both the upper-wall configuration, where the wall is above the flag (figure 1*a*i), and the lower-wall configuration, where the wall is below the flag (figure 1*a*ii), were considered. To realize sufficient deformation of the flag so that it could make contact with the rigid wall, the flag was made of silicone rubber (Young's modulus $E = 5.0 \times 10^7$ N m^{-2}, Poisson's ratio $\nu = 0.49$ and density $\rho_s = 2.3 \times 10^3$ kg m^{-3}). Significant downward deformation of the flag due to gravity was observed in the absence of flow.

The length l and width w of the flag were fixed at 10 and 5 cm, respectively, giving a constant aspect ratio $w^*(= w/l) = 0.5$ in this study. The thickness h of the flag was set to be either 0.5 or 1.0 mm. In this geometrical condition, twisting of the flag along the spanwise (crosswise) direction did not occur; that is, the deformation was two-dimensional, restricted to the x–y plane. Because the flag density ρ_s, air density ρ_f ($= 1.22$ kg m^{-3}) and flag length l were held constant, the mass ratio $m^*(= \rho_s h/\rho_f l)$ only varied with the flag thickness h; $m^* = 9.58$ and 19.16. The distance from the flagpole to the wall, d, was the main parameter in determining the flag behaviour in the present study

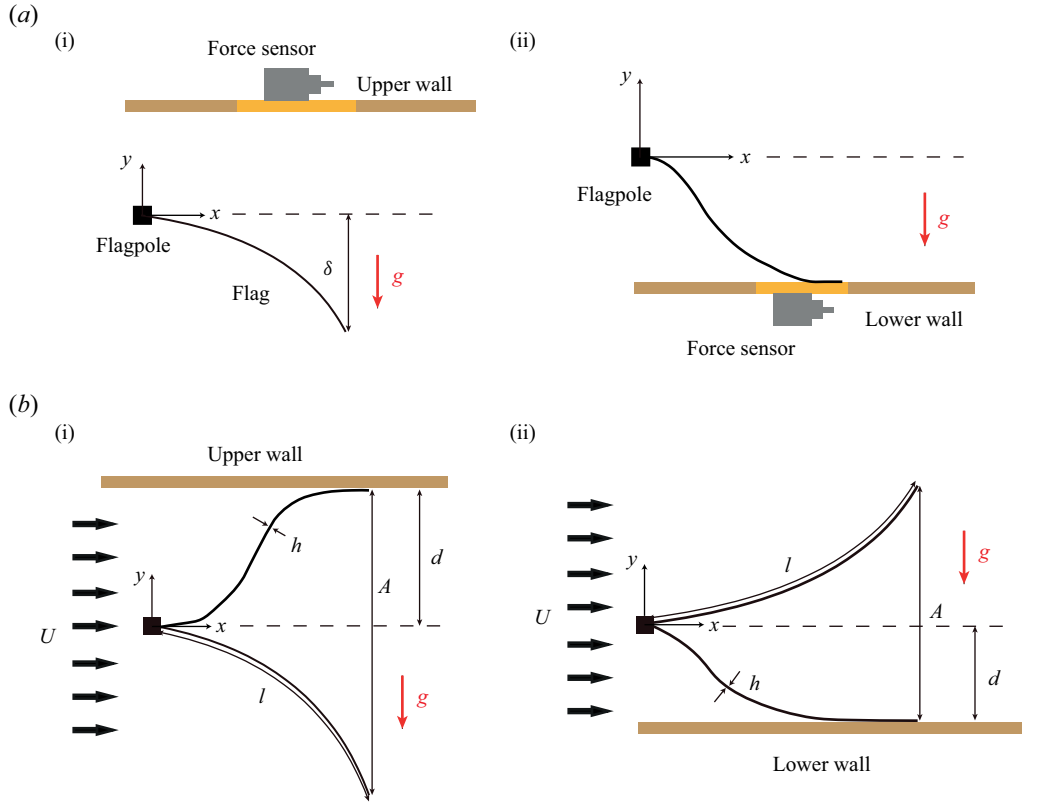

Figure 1. (*a*) Static equilibrium state of the flag in the absence of free stream: (i) upper-wall configuration and (ii) lower-wall configuration. (*b*) Definitions of geometric parameters and shapes of the fluttering flag in the presence of a free stream. The red arrows indicate the direction of gravity, and the yellow parts in (*a*i) and (*a*ii) denote the wall segment attached to the force sensor.

(figure 1*b*), and the wall distance ratio was defined as $d^* = d/l$. Within the free-stream velocity range of our set-up, contact did not occur when d^* was greater than 0.5 in either the upper-wall or lower-wall configuration. Thus, the wall distance ratio d^* was varied between 0.10 and 0.45 in increments of 0.05.

To capture the flag motion, one side edge of the flag was painted white, and the rest was painted black. The background of the test section was covered with black paper to highlight the white edge. The flag was illuminated by halogen lamps, and flag images were recorded at a sampling rate of 250 frames per second by a high-speed camera (FASTCAM MINI UX50, Photron Inc.) mounted on the side of the test section. The recorded images were processed with MATLAB (Mathworks Inc.) to acquire the position data of the flag.

To quantitatively analyse the contact process of the flag, we also measured the force generated by the collision of the flag with the rigid wall. A piezoelectric force sensor (97112B quarts, Kistler Inc.) was attached to a separate small segment (50 mm × 50 mm) of the wall (figure 1*a*). The voltage signal from the force sensor was sampled at a rate of 10 kHz and filtered using a band-pass filter with a lower cutoff frequency of 1 Hz and a higher cutoff frequency of 500 Hz through a signal conditioner (482A21, PCB Piezotronics Inc.). The contact force was measured three times under the same conditions to ensure the repeatability of the force data. The time history of the contact force exhibited periodic peaks during periodic contact and separation of the flag. We defined the average

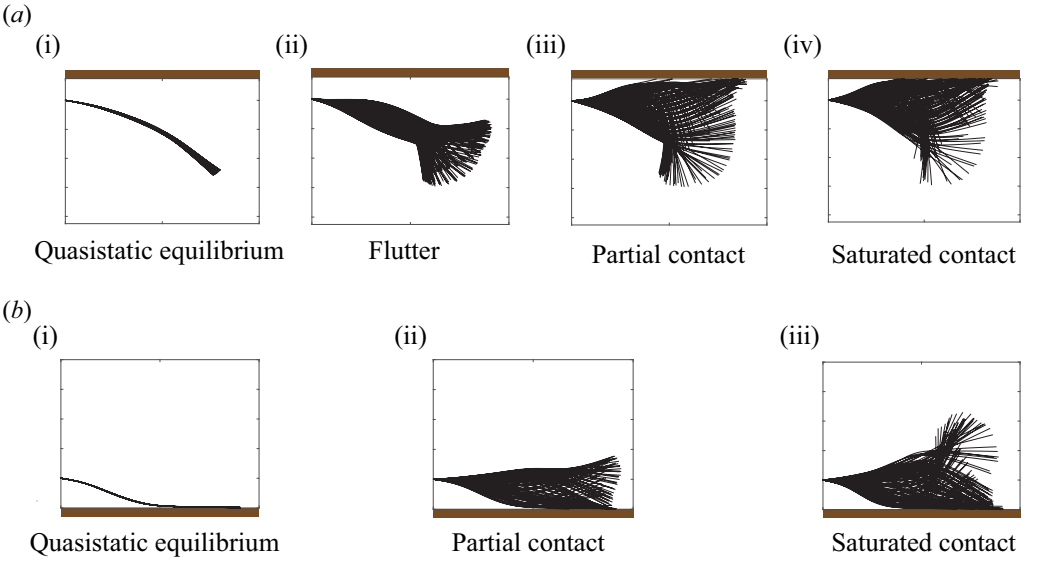

Figure 2. (*a*) Superimposed images of the flag for the upper wall: (i) quasistatic equilibrium mode; (ii) flutter mode; (iii) partial contact mode; (iv) saturated contact mode. (*b*) Superimposed images of the flag for the lower wall: (i) quasistatic equilibrium mode; (ii) partial contact mode; (iii) saturated contact mode. See supplementary movies 1 and 2 for (*a*) and (*b*), respectively.

of force peaks for 10 oscillation cycles as $F_{c,p}$. Among three repeated trials, the difference in the magnitude of $F_{c,p}$ was within 5 % of the average value of the three trials.

3. Results and discussion

3.1. *Mode classification*

Four distinct modes of the flag are identified according to the free-stream velocity U and the distance d between the wall and the flagpole. The classification of the modes depends on the location of the wall. When a wall is installed above the flag, the wall distance d does not affect the initial configuration of the flag at $U = 0$ (figure 1*a*i), and the initial configuration is determined by gravity and the bending rigidity of the flag. Under a fluid flow, the fluid force exerted on the flag is balanced by the weight and internal bending force of the flag, yielding quasistatic deformation of the sheet with negligible vibrations: quasistatic equilibrium mode in figure 2(*a*i) and supplementary movie 1 available at https://doi.org/10.1017/jfm.2023.931. As U increases beyond a critical value U_{c1}, the flag becomes unstable and flutters asymmetrically due to the effect of gravity (figure 2*a*ii). With a further increase in U, the amplitude of the flag increases accordingly, and the flag begins to contact the wall periodically (figures 2*a*iii and 2*a*iv).

By contrast, when a wall is installed below the flag, the wall distance d affects the initial configuration of the flag at $U = 0$ (figure 1*a*ii), and the flag is in contact with the wall in the entire range of d examined in this study. As U increases, the quasistatic equilibrium state directly transitions to the periodic contact state at a critical velocity U_{c1} (figure 2*b* and supplementary movie 2). In the postequilibrium state, the flutter mode without contact, which corresponds to figure 2(*a*ii) for the upper wall, does not occur, and the flag contacts the wall periodically once it begins to flutter. The chaotic contact mode reported in the

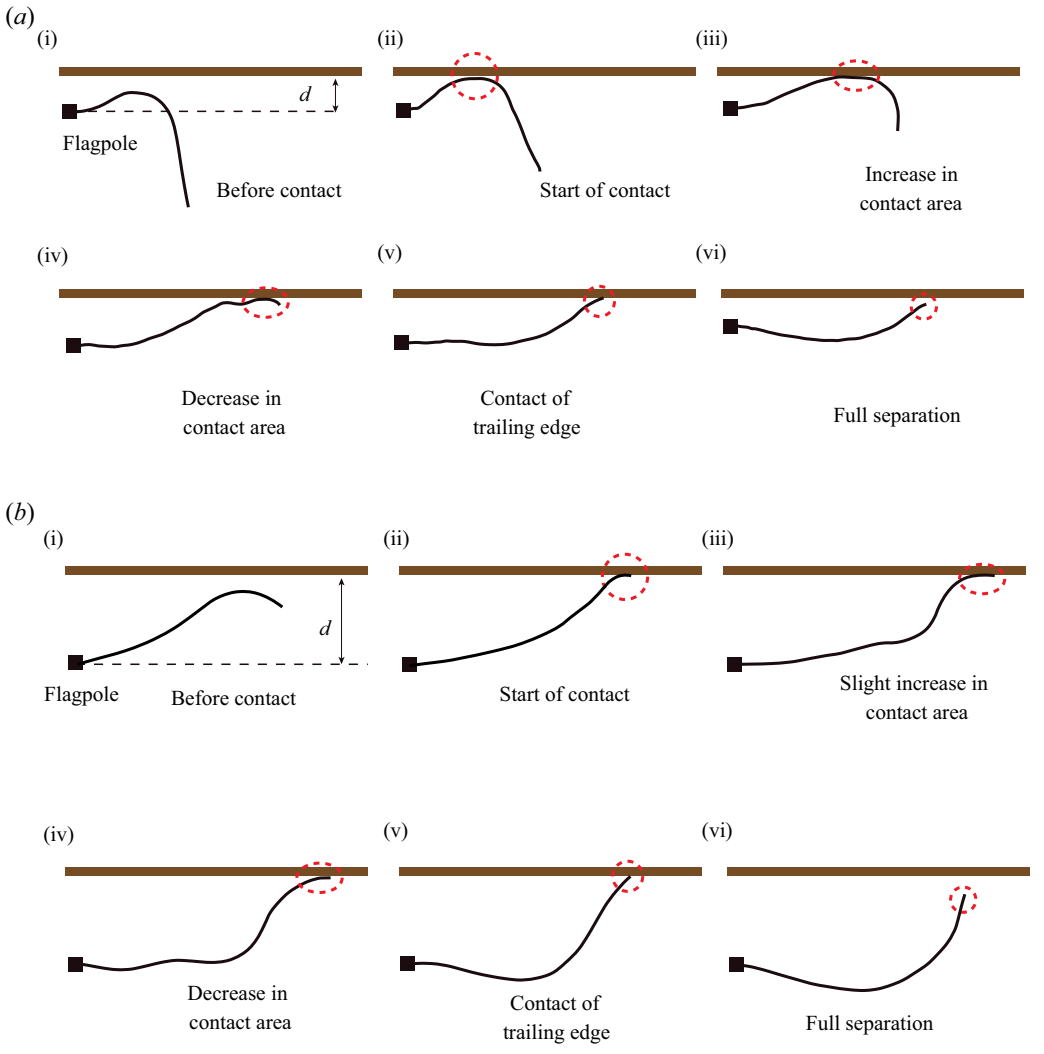

Figure 3. Sequences of contact process for the upper wall: (*a*) small wall distance d and (*b*) large d.

previous studies with a vertical flag and a nearby vertical wall (Bae *et al.* 2014; Lee *et al.* 2021) is not observed for the flow velocity range available in the present study.

The general sequence of contact between the flag and the wall is illustrated in figure 3. In the case of an upper wall, the contact process is determined by how close the flagpole is to the wall, because the downward gravitational force interrupts the contact. For small d ($d \leq 2.0$ cm), the contact commences at a specific point in the middle of the flag and propagates downstream, increasing the area of contact (figures 3*a*i–3*a*iii). The contact area then decreases until contact occurs at the trailing edge of the flag (figures 3*a*iv and 3*a*v). Finally, the flag is fully separated from the wall (figure 3*a*vi). This contact process is similar to when a flag makes contact under the condition that the influence of gravity is negligible, e.g. a vertical flag near a vertical wall (Bae *et al.* 2014). However, when d is large ($d \geq 2.5$ cm), contact begins near the trailing edge of the flag and propagates only

slightly upstream (figures 3*b*i–3*b*iii). The subsequent process is similar to the small-d case until the flag is fully separated from the wall (figures 3*b*iv–3*b*vi).

For the lower wall, the contact process is similar to that of the upper wall with small d, as depicted in figure 3(*a*). Regardless of d, the contact starts at a specific point in the middle of the flag and propagates downstream. Gravity acting downwards makes the contact begin in the middle of the flag and propagate along the streamwise direction, even for the large-d case. This is the distinction in the contact process with a large d between the upper wall and lower wall. In summary, as our flag model is horizontal and sufficiently soft for large deflection, the influence of gravity is sufficiently strong that the distance d and the location of the wall significantly affect the contact process.

The contact state is subdivided into partial and saturated contact modes for both the upper and lower walls (figure 2) according to the dramatic change in the contact process across a threshold of U. To analyse the contact process in depth, two quantities are considered. The location at which contact begins is identifiable from the images, and the streamwise distance between the leading edge and the first contact point is defined as X_c (figure 4*a*). In addition, the duration from when the flag begins to contact the wall at a certain point to when it becomes fully separated from the wall is defined as T_c; $T_c = 0$ in the quasistatic equilibrium and flutter modes. Because the dynamics of our model during contact are strongly affected by gravity and wall distance and is generally different from that of a vertical flag with a nearby vertical wall, the new terms for contact modes are introduced to describe the contact process more properly instead of employing the terms used by Lee *et al.* (2021).

Irrespective of the wall location (either upper or lower) and distance d, X_c gradually decreases with increasing U, implying that a greater area of the flag contacts the wall during the contact process (figure 4*b*): partial contact mode. However, above a certain U, X_c resides in a narrow range. This saturation of X_c indicates that the contact is fully developed: saturated contact mode. Furthermore, the contact duration T_c increases rapidly with U in the contact state, before reaching a plateau (figure 4*c*). For the same model configuration (upper or lower wall), wall distance d and flag thickness h, the threshold value of U beyond which T_c remains almost unchanged coincides with the threshold corresponding to the saturation of X_c (figure 4*b*,*c*). In this study, the critical velocity for the transition between the partial and saturated contact modes are termed U_{c2} for both the upper and lower walls; the critical conditions for mode transitions are discussed in § 3.2.

3.2. *Mode distribution and critical velocity*

To quantitatively analyse the interaction between a flag and a surrounding fluid, many previous studies have adopted a dimensionless flow velocity $U^* = U(\rho_f l^3/B)^{1/2}$, which represents the ratio of the fluid force exerted on the flag to its internal bending force (e.g. Connell & Yue 2007; Eloy *et al.* 2008; Kim *et al.* 2013, 2017). However, the gravitational force is also important in our flag model. The bending force per unit width, F_b, scales as B/l^2 for large deflections, where the bending stiffness per unit width $B = Eh^3/12(1-\nu^2)$ and the gravitational force per unit width F_g scales as $\rho_s ghl$. The ratio of the two forces, $F_b/F_g \sim B/\rho_s ghl^3$, is 0.24 for a flag thickness h of 1 mm and 0.06 when h is 0.5 mm. The gravitational force is dominant over the bending force in our model, making it acceptable to define the dimensionless flow velocity based on the ratio of fluid force to gravitational force.

As mentioned in § 3.1, for the upper-wall case, the distance between the wall and the flagpole, d, does not affect the initial configuration of the flag at $U = 0$. The fluid force exerted on the flag scales with the vertical downward deflection δ of the flag trailing edge,

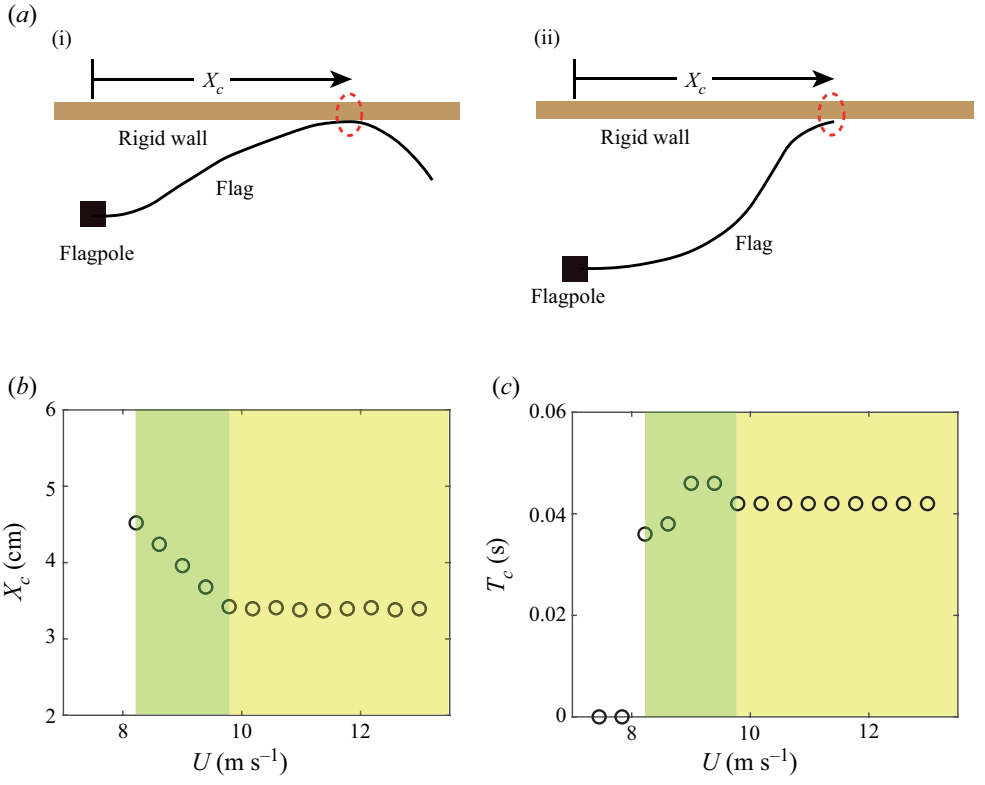

Figure 4. (*a*) Definition of streamwise distance X_c between the leading edge and the first contact point for (i) small d and (ii) large d. Here (*b*) X_c and (*c*) contact duration T_c with respect to free-stream velocity U for the upper wall ($[d, h] = [1.5\ \text{cm}, 1.0\ \text{mm}]$). The green and yellow areas denote the partial contact and saturated contact modes, respectively.

from the horizontal line on the flagpole, in the absence of flow (figure 1*a*i). Even for the fluttering flag, the fluid force is more relevant to δ than to d because δ is greater than d in our model. The fluid force per unit width then scales as $F_f \sim \rho_f U^2 \delta$. In the previous studies regarding the interaction of an elastic sheet with a fluid flow, the large deflection of the sheet was scaled as the length of the elastic sheet (Jung, Song & Kim 2021; Kim *et al.* 2021; Lee, Joung & Kim 2022). Because of the use of soft material in this study, the deflection of the flag is comparable to the flag length in the absence of flow and sufficiently large in the most range of the quasistatic equilibrium state. Therefore, δ scales as the flag length l, leading to $F_f \sim \rho_f U^2 l$.

This scaling of the fluid force is the same as that found in previous studies on fluttering flags in the absence of gravity and contact. With the gravitational force per unit width $F_g \sim \rho_s g h l$, a new dimensionless flow velocity for the upper wall is suggested as

$$U^* = U\left(\frac{\rho_f}{\rho_s g h}\right)^{1/2} = Fr(m^*)^{-1/2}, \tag{3.1}$$

which indicates the relative magnitude of the fluid force with respect to the gravitational force. Here U^* can also be defined using the Froude number $Fr(= U/(gl)^{1/2})$ and the mass ratio $m^*(= \rho_s h/\rho_f l)$.

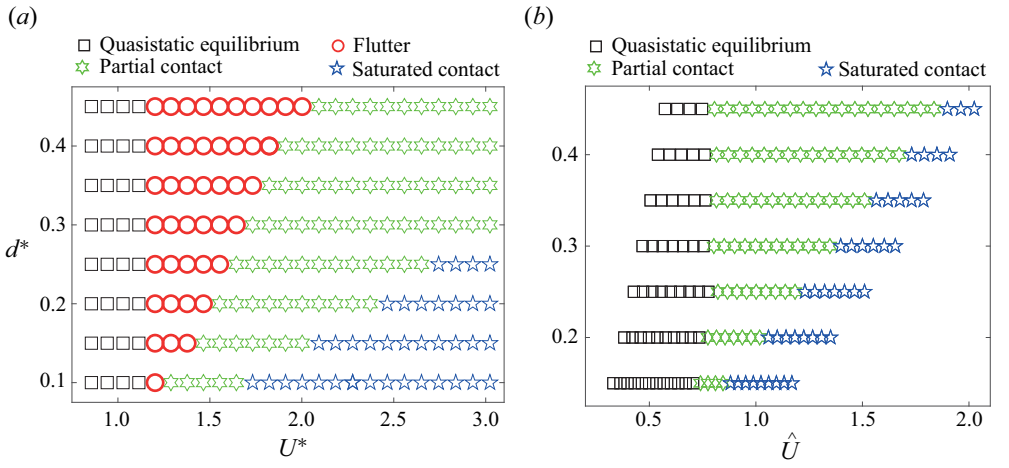

Figure 5. (*a*) Distribution of four modes in terms of U^* in (3.1) and d^* for the upper wall ($m^* = 19.16$). (*b*) Distribution of three modes in terms of $\hat{U}$ in (3.2) and d^* for the lower wall ($m^* = 19.16$).

For the lower-wall case, it is clear that the fluid force F_f is influenced by d because the flag is initially in contact with the wall and d determines the initial configuration of the flag at $U = 0$; note that we limit the range of d so that the flag is in contact with the lower wall at $U = 0$. The fluid force scales reasonably as $F_f \sim \rho_f U^2 d$, while the scaling of the gravitational force F_g is the same as in the upper-wall case. Considering the ratio of the two forces, a new dimensionless flow velocity for the lower wall is defined as

$$\hat{U} = U\left(\frac{\rho_f d}{\rho_s g h l}\right)^{1/2} = Fr(m^*)^{-1/2}(d^*)^{1/2}, \tag{3.2}$$

where $\hat{U}$ can also be expressed in terms of Fr, m^* and the wall distance ratio $d^*(= d/l)$.

Using the dimensionless flow velocity (U^* for the upper wall and $\hat{U}$ for the lower wall) and the distance ratio $d^*(= d/l)$, the flag modes described in § 3.1 are illustrated in figure 5. For the upper wall (figure 5*a*), the dimensionless first critical velocity U^*_{c1} between the quasistatic equilibrium mode and flutter mode is independent of d^*. Because the flag is deflected downwards and the initial configuration of the flag is independent of the wall distance, d^* is not a factor in the transition between these two modes. However, the dimensionless second critical velocity U^*_{c2} between the partial contact mode and saturated contact mode increases monotonically with d^*. As d^* becomes greater, the transition to the saturated contact mode occurs at a higher dimensionless flow velocity U^*. Another critical velocity for the transition between the flutter mode and partial contact mode, which appears only for the upper wall, is not examined because the present study aims to compare critical conditions for the upper-wall and lower-wall cases.

The trends in the dimensionless critical velocities for the lower wall are similar to those for the upper wall, although we have different definitions of the dimensionless flow velocity, (3.1) for the upper wall and (3.2) for the lower wall. By adopting a dimensionless flow velocity appropriate for each configuration, it is possible to characterize the mode transition trends consistently. In figure 5(*b*), the dimensionless first critical velocity $\hat{U}_{c1}$ exhibits little variation with d^*, whereas the dimensionless second critical velocity $\hat{U}_{c2}$ increases monotonically with d^*. Because the wall distance d is included in the definition of $\hat{U}$ in (3.2), the relationship between the dimensional wall distance d and the dimensional

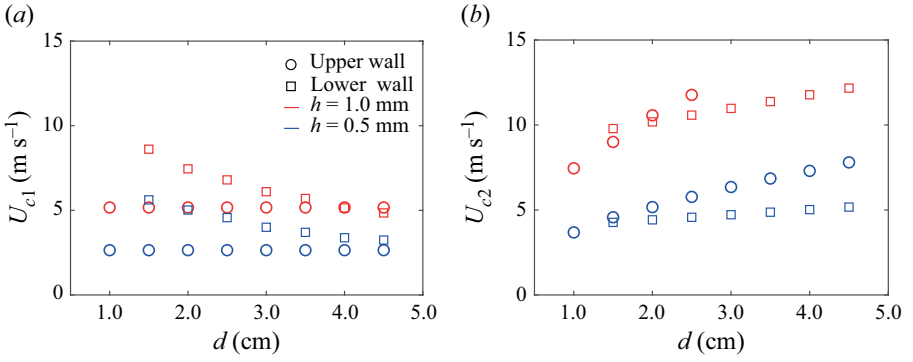

Figure 6. (*a*) First critical velocity U_{c1} and (*b*) second critical velocity U_{c2} with respect to wall distance d for both the upper-wall and lower-wall configurations: $h = 1.0$ mm ($m^* = 19.16$) and $h = 0.5$ mm ($m^* = 9.58$).

critical velocities U_{c1} and U_{c2}, with the other dimensional parameters unchanged, cannot be directly captured from figure 5(*b*).

In contrast to our upper-wall configuration and the vertical flag/wall configuration of Lee *et al.* (2021) in which the first critical velocity U_{c1} is insensitive to d for $d = 1.5$–5.5 cm and $l = 5$–16 cm, U_{c1} decreases monotonically with increasing d for our lower-wall configuration, over the entire range of d considered in this study (figure 6*a*). As d increases, a greater fluid force is imposed on the flag, making the transition to the postequilibrium state easier. For the lower wall with the smallest $d = 1.0$ cm, the gap between the flagpole and the wall is too narrow, and the fluid force is not sufficient to induce the transition to the postequilibrium state. For this reason, the value of U_{c1} is omitted for $d = 1.0$ cm in figure 6(*a*). In this study, the range of d for the lower wall is smaller than the initial downward deflection δ of the trailing edge for the upper wall (figure 1*a*i). The magnitude of the fluid force exerted on the sheet is smaller for the lower wall than for the upper wall at a given U in the quasistatic equilibrium state. Consequently, U_{c1} for the lower wall exceeds that for the upper wall under the same wall distance d and flag thickness h (figure 6*a*).

As the second critical velocity U_{c2} is a threshold that subdivides the postequilibrium state into partial and saturated contact modes, its analysis should be conducted from a different point of view to that of U_{c1} related to the equilibrium state. When the flag is in the equilibrium state, the fluid force scales with the flag length l for the upper wall and the wall distance d for the lower wall. However, when the flag reaches the periodic contact modes, the effect of the incoming flow is mainly determined by the oscillation amplitude of the flag, which is generally comparable to or greater than the wall distance d. Therefore, the relationship between U_{c2} and d is expected to have a similar tendency, regardless of the wall location (upper wall or lower wall). Indeed, U_{c2} increases monotonically with respect to d for both wall locations (figure 6*b*). When the fluttering flag contacts the wall periodically, the y-coordinate of the flag's centre of mass, y_G, changes periodically as well, and the vertical displacement of y_G increases with d. The flag requires more potential energy to make saturated contact. As the potential energy of the flag comes from the kinetic energy of the incoming flow, U_{c2} increases with d.

Although the tendency of U_{c2} with respect to d is similar between the two wall locations, the magnitude of U_{c2} at the same d is clearly affected by the wall location, and U_{c2} for the upper wall exceeds that for the lower wall in most conditions (figure 6*b*). This is because, for the upper wall, the presence of gravity acting in the opposite direction interrupts the fully developed contact of the flag with the wall. Moreover, for both wall locations, U_{c2}

becomes greater with increasing flag thickness h for a given d because a greater fluid force is necessary for the heavier flag (figure 6*b*); this is also true for U_{c1} (figure 6*a*). This trend with respect to h can be attributed to the increase in internal bending force induced by the enhanced bending stiffness, in addition to the increase in the gravitational force.

Thus far, we have reported the general trends of the critical velocities. Next, using simple scaling analysis, we derive quantitative relationships between the wall distance and two critical velocities (U_{c1} and U_{c2}) for the upper wall and lower wall, respectively. For the upper wall, the fluid force acting on the flag is balanced by the gravitational and bending forces in the quasistatic equilibrium. As mentioned above, the gravitational force is generally more significant than the bending force for our flag model. Therefore, it is assumed that the transition from quasistatic equilibrium mode to flutter mode is initiated when the fluid force becomes greater than the gravitational force. The fluid force per unit width $F_f \sim \rho_f U^2 l$ and the gravitational force per unit width $F_g \sim \rho_s g h l$ obey the following scaling relations at the first critical condition $U = U_{c1}$:

$$\rho_f U_{c1}^2\, l \sim \rho_s g h l, \tag{3.3a}$$

$$Fr_{c1}(m^*)^{-1/2} \sim \text{const.} \tag{3.3b}$$

Corresponding to $U = U_{c1}$, the first critical Froude number is defined as $Fr_{c1} = U_{c1}/(gl)^{1/2}$. The term $Fr_{c1}(m^*)^{-1/2}$ on the left-hand side of (3.3*b*) is actually the same as U_{c1}^* in (3.1). As shown in figure 5(*a*), $Fr_{c1}(m^*)^{-1/2}$ $(= U_{c1}^*)$ is independent of d^*.

Regarding the lower wall, the wall distance d, rather than l (or δ), is the key length parameter in determining the fluid force in the equilibrium state. The fluid force $F_f \sim \rho_f U^2 d$ instead of $\rho_f U^2 l$. The gravitational force $F_g \sim \rho_s g h l$ is the same as for the upper wall. Accordingly, at $U = U_{c1}$,

$$\rho_f U_{c1}^2 d \sim \rho_s g h l, \tag{3.4a}$$

$$Fr_{c1}(m^*)^{-1/2}(d^*)^{1/2} \sim \text{const.} \tag{3.4b}$$

The contact force from the lower wall is neglected because only the trailing edge of the flag is in contact during the transition between the quasistatic equilibrium and partial contact modes. The term $Fr_{c1}(m^*)^{-1/2}(d^*)^{1/2}$ on the left-hand side of (3.4*b*) is identical to $\hat{U}_{c1}$ in (3.2). Relation (3.4*b*) is consistent with the experimental results in figure 5(*b*), in which $Fr_{c1}(m^*)^{-1/2}(d^*)^{1/2}$ $(= \hat{U}_{c1})$ exhibits little variation with respect to d^*. To validate (3.4*b*), figure 6(*a*) is reconstructed in figure 7 using dimensionless variables (Fr_{c1}, m^*, and d^*). The fitting curve $Fr_{c1}(m^*)^{-1/2} = 0.75(d^*)^{-1/2}$ from scaling relation (3.4*b*) is in good agreement with the experimental results.

As for the scaling analysis of the second critical velocity U_{c2}, it is more appropriate to consider energy rather than force because U_{c2} is defined in the midst of the postequilibrium state. In our model, four energy quantities of the flag need to be accounted for: strain energy (E_s); kinetic energy ($E_{k,flag}$); potential energy (E_p); and the energy dissipated during the contact process (E_c). As scaling analysis is based on the relation between two dominant physical quantities, it is necessary to identify the dominant energy component of the flag, which is balanced with the fluid kinetic energy input imposed on the flag ($E_{k,fluid}$).

We first calculate each energy component from the experimental data to compare the magnitudes of the energy components. The strain energy E_s of the flag per unit width is defined as $E_s = \frac{1}{2}B\int_0^l \kappa^2\,\mathrm{d}s$, where κ $(= (\mathrm{d}^2y/\mathrm{d}x^2)/[1 + (\mathrm{d}y/\mathrm{d}x)^2]^{3/2})$ is the curvature of the flag. The curvature is computed from the position data obtained from the images. The sheet is discretized equally into 200 segments along its length. For each segment, the

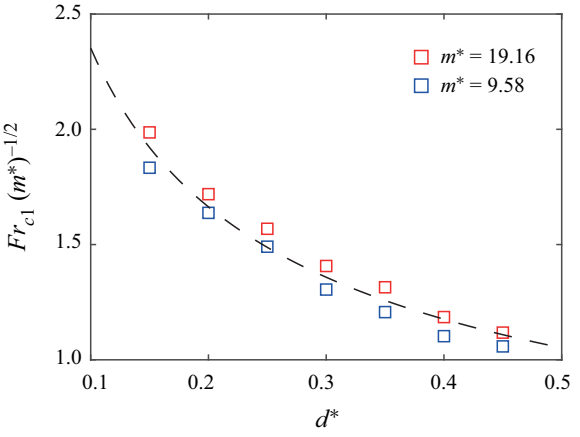

Figure 7. First critical condition $Fr_{c1}(m^*)^{-1/2}$ with respect to distance ratio d^* for the lower wall. The symbols denote experimental data, and the black dashed line denotes the fitting curve from scaling relation (3.4*b*).

central difference scheme is used to acquire $\mathrm{d}^2y/\mathrm{d}x^2$ and $\mathrm{d}y/\mathrm{d}x$. In addition to the bending energy, the stretching energy may be considered for the strain energy. However, the tension acting on the flag and the resultant change in the flag length are negligible. For this reason, the stretching energy is assumed to be zero. The kinetic energy $E_{k,flag}$ of the flag per unit width is defined as $E_{k,flag} = \frac{1}{2}\rho_s h \int_0^l v^2\,\mathrm{d}s$, where v $(= [(\mathrm{d}x/\mathrm{d}t)^2 + (\mathrm{d}y/\mathrm{d}t)^2]^{1/2})$ is the velocity magnitude of the flag. For each segment, the central difference scheme is used to obtain $\mathrm{d}x/\mathrm{d}t$ and $\mathrm{d}y/\mathrm{d}t$. The potential energy E_p of the flag per unit width is defined as $\rho_s g h \int_0^l y\,\mathrm{d}s$, where y is the vertical position of the flag. As $y = 0$ is set at the leading edge (flagpole), as shown in figure 1, the potential energy can be negative when the flag is located below the flagpole.

The three energy components (E_s, $E_{k,flag}$ and E_p) of the flag at the second critical velocity are compared in figure 8. Although the energy is dissipated as acoustic energy during the contact process, the overall magnitude of the dissipated energy E_c appears to be negligible because the material of the flag does not absorb energy, and the duration of the contact is very small compared with the period of flutter. The peak-to-peak value of E_p in one cycle is dominant over those of the other energy components for both the upper and lower walls. Although figure 8 presents the data at the second critical condition for two specific cases of $[d, h] = [1.5\ \mathrm{cm}, 1.0\ \mathrm{mm}]$, the potential energy of the flag is found to be dominant in the postequilibrium state regardless of the wall location, d, and h. Based on this result, it is reasonable to consider the fluid kinetic energy $E_{k,fluid}$ and the potential energy of the flag E_p for scaling analysis.

The two energy quantities $E_{k,fluid}$ and E_p should be balanced in a cycle-averaged sense in terms of scaling: $\bar{E}_{k,fluid} \sim \bar{E}_p$. The kinetic energy $E_{k,fluid}$ of the fluid per unit width is defined as the total power imposed on the sheet by the uniform flow during a cycle. Here $E_{k,fluid} = \int_0^T \int_0^l \boldsymbol{F_f}\cdot\boldsymbol{v}\,\mathrm{d}s\,\mathrm{d}t$, where $\boldsymbol{F_f}$ is the fluid force vector acting on the flag per unit area, $\boldsymbol{v}$ is the velocity vector of the flag and T is the period of flutter. From this integral expression, the fluid kinetic energy can be scaled without using the flutter period T. The fluid force $\boldsymbol{F_f}$ scales as $F_f \sim \rho_f U^2$, the dynamic pressure induced by the free-stream velocity. Here $\int_0^T \boldsymbol{v}\,\mathrm{d}t$ scales as the peak-to-peak oscillation amplitude A of the flag, and $\int_0^l \mathrm{d}s = l$. Consequently, $\bar{E}_{k,fluid} \sim \rho_f U^2\, lA$. At postequilibrium, the

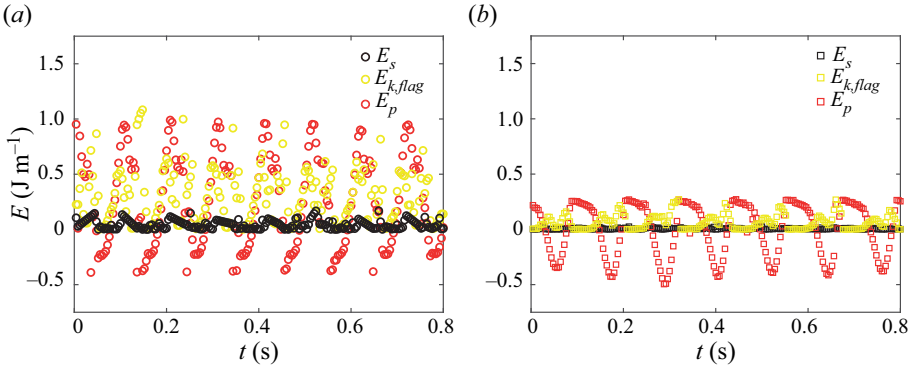

Figure 8. Time histories of strain energy E_s (black), kinetic energy $E_{k,flag}$ (yellow) and potential energy E_p (red) of the flag per unit width at the second critical velocity U_{c2} for the (*a*) upper wall and (*b*) lower wall. $[U, d, h] = [9.79\ \text{m s}^{-1}, 1.5\ \text{cm}, 1.0\ \text{mm}]$ for the upper wall and $[10.18\ \text{m s}^{-1}, 1.5\ \text{cm}, 1.0\ \text{mm}]$ for the lower wall.

vertical displacement Δy_G for the centre of the flag determines the potential energy. As d increases, the magnitude of Δy_G required for saturated contact increases, which indicates that the potential energy may scale with d. Indeed, $\bar{E}_p$ computed from our experimental results tends to increase linearly with d for both the upper wall and lower wall; see Appendix A. Thus, the cycle-averaged potential energy of the flag per unit width is regarded as $\bar{E}_p \sim \rho_s ghld$.

As the peak-to-peak amplitude A defined in figure 1(*b*) is a dependent variable that should be obtained from experiments, it is necessary to employ a different length scale based on the input parameters. For the upper wall, the oscillation amplitude of the flag is almost independent of d, and $A^*(= A/l)$ converges to a specific value as the dimensionless flow velocity increases (as reported in § 3.3). Hence, it is reasonable to argue that A scales as the flag length l, leading to $\bar{E}_{k,fluid} \sim \rho_f U^2 l^2$. At the second critical condition $U = U_{c2}$ of the upper wall, the following scaling relations are established from the energy balance $\bar{E}_{k,fluid} \sim \bar{E}_p$:

$$\rho_f U_{c2}^2 l^2 \sim \rho_s ghld, \tag{3.5a}$$

$$Fr_{c2}(m^*)^{-1/2} \sim (d^*)^{1/2}, \tag{3.5b}$$

where the second critical Froude number $Fr_{c2} = U_{c2}/(gl)^{1/2}$ and $Fr_{c2}(m^*)^{-1/2} = U_{c2}^*$. As depicted in figure 5(*a*), U_{c2}^* increases monotonically with d^*.

In contrast to the upper wall, the peak-to-peak amplitude A of the flag for the lower wall is distinctly affected by d; a detailed explanation will be given in § 3.3. Thus, the effect of d must be included when scaling the oscillation amplitude. The amplitude of the flag can be divided into two parts based on $y = 0$ (figure 1*b*ii). In the lower-wall case, the amplitude in the region $y < 0$ is equal to d, and we assume that the amplitude in the region $y > 0$ is proportional to the flag length l, having the form αl with the proportional constant α to be determined later. As for the amplitude scale, $A \sim d + \alpha l$ is adopted instead of $A \sim l$. From the energy balance between $\bar{E}_{k,fluid} \sim \rho_f U^2 l(d + \alpha l)$ and $\bar{E}_p$, at the second critical condition $U = U_{c2}$ of the lower wall,

$$\rho_f U_{c2}^2\, l(d + \alpha l) \sim \rho_s ghld, \tag{3.6a}$$

$$Fr_{c2}(m^*)^{-1/2}(d^*)^{1/2} \sim d^*(d^* + \alpha)^{-1/2}. \tag{3.6b}$$

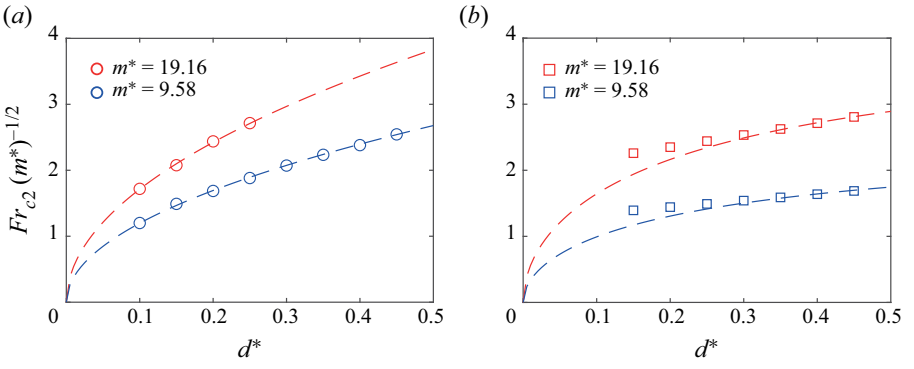

Figure 9. Second critical condition $Fr_{c2}(m^*)^{-1/2}$ with respect to wall distance ratio d^* for the (a) upper wall and (b) lower wall. The symbols denote experimental data, and the dashed lines denote the fitting curves from scaling relation (3.5b) for (a) and from scaling relation (3.6b) for (b).

Here, $Fr_{c2}(m^*)^{-1/2}(d^*)^{1/2} = \hat{U}_{c2}$. Relation (3.6$b$) captures the trend of the experimental results, with $\hat{U}_{c2}$ increasing monotonically with d^* in figure 5(b).

The second critical velocity U_{c2} in figure 6(b) is reconstructed in dimensionless form, using Fr_{c2}, m^* and d^*, in figure 9. For a given m^*, the fitting curves from scaling relations (3.5b) and (3.6b) are also included. For the upper wall in figure 9(a), $Fr_{c2}(m^*)^{-1/2} = C(d^*)^{1/2}$ from (3.5b), where the fitting constant C is 5.42 for $m^* = 19.16$ and 3.76 for $m^* = 9.58$. The values predicted from the scaling analysis are in good agreement with the experimental results. Note that the constant C depends on m^*, although m^* is explicitly included in the scaling relation. Although the kinetic energy of the flag is not as dominant as the potential energy of the flag and is not included on the right-hand side of (3.5a), it is not actually negligible according to figure 8. The kinetic energy of the flag is proportional to the mass ratio (flag thickness h) of the flag. Therefore, the dimensionless velocity $U^*_{c2}(= Fr_{c2}(m^*)^{-1/2})$ is expected to increase as the kinetic energy of the flag becomes stronger (i.e. when m^* increases), which is demonstrated experimentally in figure 9(a).

For the lower wall (figure 9b), α in (3.6b) is obtained empirically from the experimental data in the postequilibrium state; $\alpha = (A - d)/l$. The value of α averaged over seven different d^* cases is 0.55 for both $m^* = 19.16$ and 9.58 (see Appendix B). Thus, $Fr_{c2}(m^*)^{-1/2} = C(d^*)^{1/2}(d^* + 0.55)^{-1/2}$ from (3.6b), where the fitting constant C is 4.19 for $m^* = 19.16$ and 2.52 for $m^* = 9.58$. The constant C varies with respect to m^*, as for the upper wall. When d^* is relatively low ($d^* = 0.15$), the curve of the scaling relation deviates notably from the experimental values. The value of α is fixed in the fitting process, although it varies with respect to d and U (Appendix B). If α is chosen using only the small-d^* cases, the fitting curve in figure 9(b) will be good in the small-d^* region but give poor predictions in the large-d^* region. Despite such limitations, we can successfully predict the trend of the second critical velocity by applying simple scaling relations based on energy balance.

For the given d in the range considered in this study, $l > d + \alpha l$. From the above scaling relations for $\bar{E}_{k,fluid}$ and $\bar{E}_p$, $\bar{E}_p$ of the upper wall is larger than that of the lower wall, and accordingly the peak-to-peak value of E_p in one cycle for the upper wall exceeds that of the lower wall, as exemplified in figure 8. The kinetic energy of the flag, E_k, also exhibits similar trends when compared between the upper wall and lower wall. That is, the presence of gravity and the location of the wall greatly affect the temporal distributions of the energy components of the flag as well as its critical conditions.

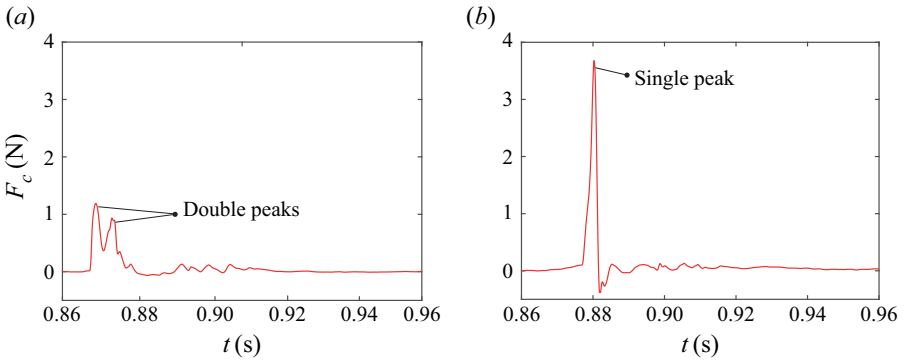

Figure 10. (*a*) Contact force F_c of partial contact mode, $[U, d, h] = [9.39\ \text{m s}^{-1},\ 3.0\ \text{cm},\ 1.0\ \text{mm}]$, and (*b*) F_c of saturated contact mode, $[U, d, h] = [11.38\ \text{m s}^{-1},\ 3.0\ \text{cm},\ 1.0\ \text{mm}]$, for the lower-wall configuration.

3.3. *Flag dynamics in postequilibrium state*

This section examines some representative quantities, such as the contact force, oscillation amplitude and oscillation frequency, of the postequilibrium flag dynamics. The contact force exerted on the wall by the fluttering flag, which is measured with a load cell, exhibits periodic peaks following the oscillation period of the flag (figure 10). The temporal profile of the contact force during the contact and separation process differs between the partial and saturated contact modes and can thus be used to quantitatively distinguish the two modes, in addition to the initial contact point X_c and contact duration T_c presented in figure 4.

In the partial contact mode, the first peak appears as the flag makes contact with the wall (figure 10*a*). After the first peak, the contact force does not decrease to zero but increases again, producing a second peak with a slightly smaller magnitude than the first peak. After the second peak, the contact force returns to zero when the flag separates from the wall. The contacting parts do not separate simultaneously from the wall in the partial contact mode, but instead, some parts remain in contact while the others separate. This phenomenon leads to a relatively weak second peak. As the partial contact mode transitions to the saturated contact mode with increasing free-stream velocity U, only one stronger peak arises per cycle (figure 10*b*). In the saturated contact mode, the contacting parts separate from the wall rapidly and almost simultaneously in contrast to the partial contact mode, thereby yielding a single strong peak. Although U increases by only $1.99\ \text{m s}^{-1}$ from the partial contact mode in figure 10(*a*) to the saturated contact mode in figure 10(*b*), the peak contact force increases dramatically, from 1.1 to 3.7 N. This feature of the contact force is common regardless of the wall location and other geometric parameters; during the transition of the contact mode, two peaks become a single peak, and the magnitude at the peak increases remarkably.

With the same wall distance, the magnitude of the peak contact force $F_{c,p}$ strongly depends on whether the wall is located above or below the flag. Here $F_{c,p}$ is acquired by averaging 10 successive force peaks for contact modes. For flutter mode, the flag rarely contacts the upper wall, and thus $F_{c,p}$ is computed by dividing the sum of force peaks during 10 oscillation cycles by 10. For the lower wall, when the wall distance ratio is large (i.e. $d^* = 0.40$), sufficient fluid kinetic energy $E_{k,fluid}$ is supplied because it scales with $d + \alpha l$ according to (3.6*a*). Thus, along with the positive contribution of the downward gravitational force, the large input of the fluid kinetic energy causes $F_{c,p}$ in the lower-wall

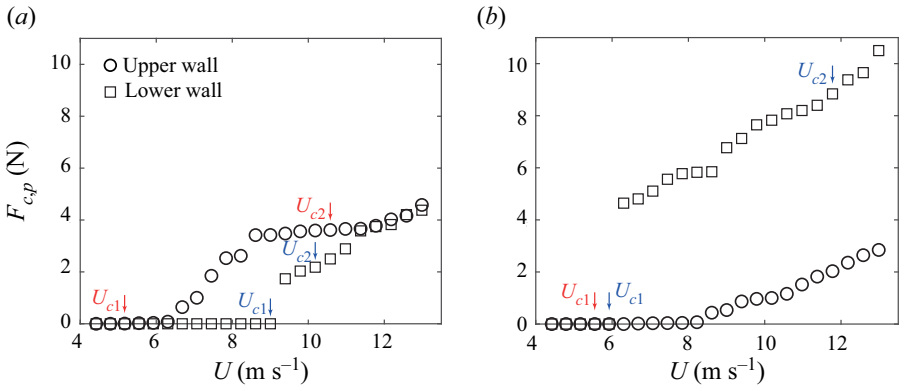

Figure 11. Peak of contact force $F_{c,p}$ versus free-stream velocity U for (*a*) $d^* = 0.20$ and (*b*) $d^* = 0.40$ ($m^* = 19.16$): upper wall (circles) and lower wall (squares). The red and blue arrows indicate critical velocities for the upper and lower walls, respectively.

case to exceed that of the upper-wall case significantly, and the difference between them becomes greater as U increases (figure 11*b*). With a large d^*, the fluttering flag must move upward to a higher location to contact the upper wall. Because the energy supplied to the flag should be used to enhance the potential energy at the moment of contact, the peak contact force $F_{c,p}$ of the upper wall decreases notably from that of the small-d^* case for the same U; compare figure 11(*b*) with figure 11(*a*).

The trend in $F_{c,p}$ differs notably for a small distance ratio $d^* = 0.20$ (figure 11*a*). $F_{c,p}$ in the lower-wall configuration is less than that of the upper-wall configuration in the intermediate range of U (= 6–11 m s^{-1}), although gravity acts to enhance the contact force for the lower wall. As mentioned above, the fluid kinetic energy $E_{k,fluid}$ scales with $d + \alpha l$ for the lower wall. In the small-d^* condition, $E_{k,fluid}$ for the lower wall is generally smaller than that of the upper wall, eventually leading to a smaller $F_{c,p}$. However, in the large-U regime ($U >$ 11 m s^{-1}), the oscillation amplitude of the lower-wall case becomes sufficiently large, resulting in greater fluid kinetic energy. Thus, $F_{c,p}$ of the lower-wall case is comparable to that of the upper wall.

The contact force for the lower wall increases rapidly at a specific free-stream velocity U (e.g. 9.39 m s^{-1} in figure 11*a* and 6.30 m s^{-1} in figure 11*b*) as the quasistatic equilibrium mode switches directly to the partial contact mode. However, for the upper wall, the contact force increases with a relatively gentle slope from a specific free-stream velocity U (e.g. 6.30 m s^{-1} in figure 11*a* and 8.22 m s^{-1} in figure 11*b*), because the quasistatic equilibrium mode does not switch directly to the partial contact mode, but goes through the flutter-mode regime. In the flutter mode, the oscillations of the flag are not perfectly periodic, and the flag can rarely contact the upper wall with small strength, which results in non-zero $F_{c,p}$, albeit minor.

From the perspective of triboelectric energy harvesting applications, it is necessary to address which wall configuration is desirable for system design. Under the same free-stream velocity and flag parameters, the lower-wall configuration appears more advantageous because gravity acts positively. However, as shown in figure 11, the desirable wall position for energy harvesting based on the peak contact force depends on the wall distance ratio d^*. According to figure 12, which presents the difference in peak contact force between the upper wall and lower wall ($\Delta F_{c,p} = F^U_{c,p} - F^L_{c,p}$), the lower wall produces the larger peak contact force over the most range of U at large distance

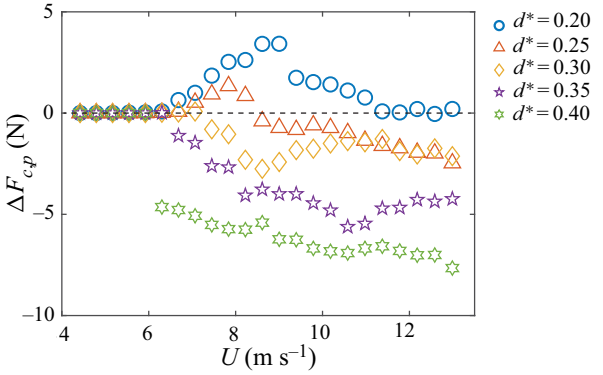

Figure 12. Difference in peak contact force $\Delta F_{c,p}(= F^U_{c,p} - F^L_{c,p})$ between the upper and lower walls with respect to free-stream velocity U ($d^* = 0.20$–0.40 and $m^* = 19.16$).

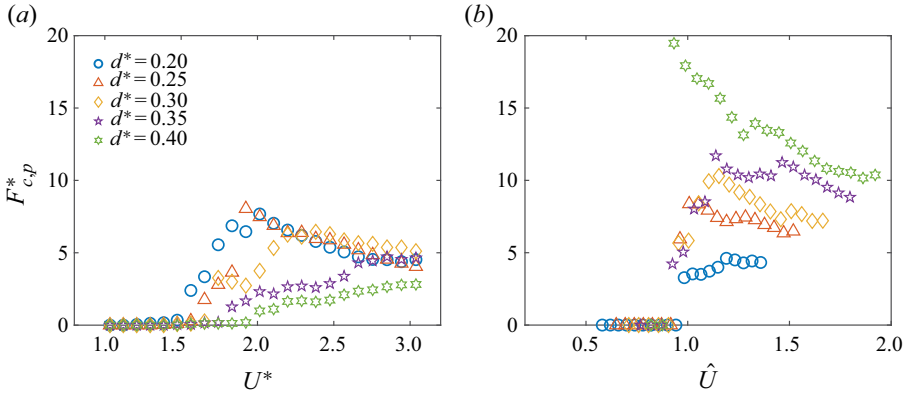

Figure 13. Contact force efficient $F^*_{c,p}$ with respect to (*a*) U^* for the upper wall and (*b*) $\hat{U}$ for the lower wall ($d^* = 0.20$–0.40 and $m^* = 19.16$).

ratios ($d^* \geq 0.30$). Conversely, the upper wall yields the larger peak contact force at a small distance ratio ($d^* = 0.20$). Furthermore, under the small distance ratio, triboelectric energy can be generated in a broader range of free-stream velocity with the upper-wall configuration because the flow velocity threshold for initiating contact is much lower than with the lower-wall configuration (figure 11*a*).

Although the dimensional $F_{c,p}$ has been used to explain the trends in the contact force, the contact force coefficient $F^*_{c,p}(= F_{c,p}/(\rho_f U^2 S))$, which is normalized by the surface area $S(= lw)$ of the flag and the free-stream velocity, may be a more suitable parameter than $F_{c,p}$ for evaluating how effectively the contact force is generated. Here $F^*_{c,p}$ is presented with respect to the dimensionless flow velocity U^* for the upper wall in figure 13(*a*) and with respect to $\hat{U}$ for the lower wall in figure 13(*b*).

The dimensional $F_{c,p}$ tends to increase monotonically with U, regardless of the wall location and wall distance (figure 11). By contrast, $F^*_{c,p}$ tends to increase and then decrease with the dimensionless flow velocity (U^* or $\hat{U}$) for most wall distance ratios (figure 13). The optimal maximum value of $F^*_{c,p}$ is clearly identified at $d^* \leq 0.30$ for the upper wall and at $d^* \geq 0.30$ for the lower wall. In the low-dimensionless-velocity regime, $F^*_{c,p}$ generally increases with the dimensionless velocity. However, as the flow velocity

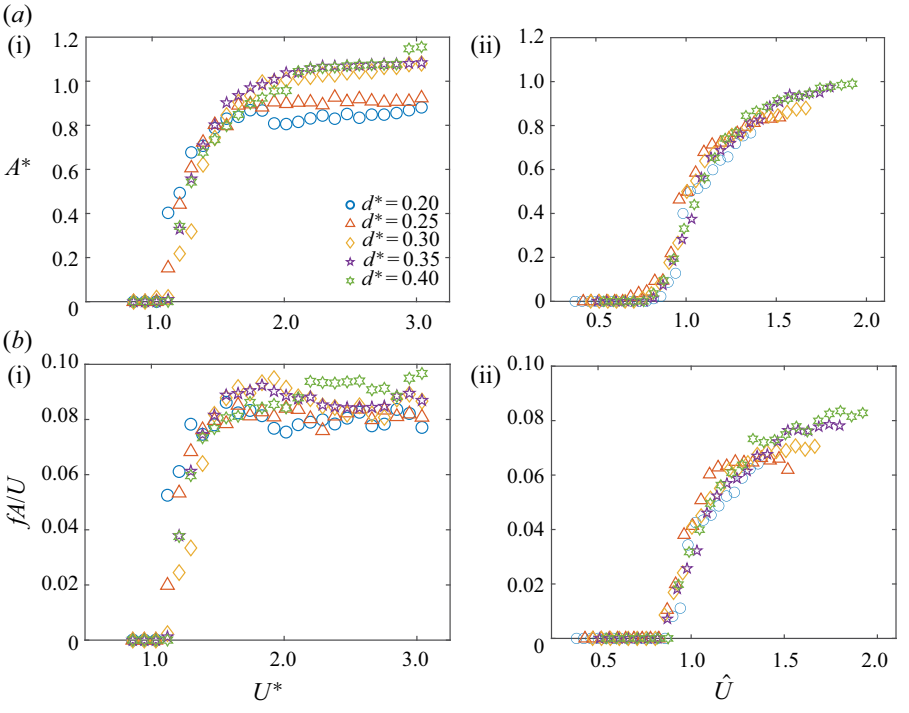

Figure 14. (*a*) Normalized peak-to-peak amplitude A^* and (*b*) Strouhal number $St(= fA/U)$ with respect to dimensionless flow velocity: (i) upper wall and (ii) lower wall ($m^* = 19.16$).

increases further, the slope of the dimensional $F_{c,p}$ versus U declines because the flag transitions from the partial contact mode to saturated contact mode and undergoes fully developed contact. Accordingly, $F^*_{c,p}$ decreases after reaching its maximum. Furthermore, figure 13 shows opposite trends of $F^*_{c,p}$ with respect to d^* between the two wall locations; $F^*_{c,p}$ tends to decrease with increasing d^* for the upper wall, while it tends to increase with increasing d^* for the lower wall. For the lower wall, the wall distance is a more important parameter in determining the magnitude of the fluid kinetic energy and contact force than for the upper wall, as mentioned above. Hence, $F^*_{c,p}$ exhibits more distinct variations among the five d^* cases at a given flow velocity.

The peak-to-peak amplitude A of the flag (figure 1*b*) is normalized by the flag length l: $A^* = A/l$. The normalized amplitude A^* displays different tendencies depending on the wall location. For the upper wall, when contact begins to occur in the partial contact mode, the amplitude above the flagpole is limited to the wall distance d (figure 1*b*i). Therefore, A^* cannot continue to increase with U^*, but converges to a certain value for each distance ratio d^* (figure 14*a*i). The converged A^* in the high-U^* regime tends to be greater for larger values of d^*, although its variations are minor between $d^* = 0.30$–0.40. By contrast, for the lower wall, the amplitude above the flagpole is not limited, and the amplitude below the flagpole is equal to d because the fluttering flag contacts the wall in all cases (figure 1*b*ii). The amplitude above the flagpole increases with the free-stream velocity U, and thus, at a given U, the peak-to-peak amplitude A becomes greater for larger values of d. Interestingly, if the dimensionless velocity $\hat{U}$, which includes d in its definition, is employed, the curves of normalized amplitude A^* collapse, and the values of A^* are similar for a given $\hat{U}$ regardless of d^* (figure 14*a*ii).

In both the upper-wall and lower-wall configurations, the dimensional frequency f tends to increase monotonically with the free-stream velocity U. To make the frequency dimensionless, the flag length l or the peak-to-peak amplitude A can be regarded as the characteristic length. In our model, A, which exhibits different trends depending on the wall location, better represents the model configuration; moreover, l is independent of the wall location. That is, the Strouhal number $St(= fA/U)$, reflecting the relative magnitude of the flutter speed of the flag tip to the free-stream velocity, is used to represent the frequency of the flag. The overall trends of St versus the dimensionless flow velocity are quite similar to those of A^* (figure 14*b*). Here St suddenly increases and thereafter becomes saturated for the upper-wall case, while it continues to increase and has a similar value irrespective of d^* for the lower-wall configuration.

For both the upper and lower walls, St is restricted below 0.10, which is markedly smaller than $St(= 0.20–0.40)$ for a vertical flag with negligible gravity effects near a vertical wall (Lee *et al.* 2021) and a typical flag model without an adjacent wall and gravity effects (Shelley, Vandenberghe & Zhang 2005; Connell & Yue 2007). Compared with the previous flag models without gravity, a significant portion of the fluid kinetic energy is converted into the potential energy of the flag, thereby reducing the kinetic energy of the flag. Hence, the flutter speed of the flag becomes relatively low compared with the previous flag models without gravity for a given free-stream velocity, which eventually results in a decrease in St. In contrast, the range of the normalized amplitude A^* in our model is comparable to that of previous flag models, $A^* = 0.4–1.0$ (Connell & Yue 2007; Eloy *et al.* 2008; Virot, Amandolese & Hémon 2013; Lee *et al.* 2021), because the downward deflection of the flag by gravity offsets the negative effect of the reduced kinetic energy of the flag on the oscillation amplitude.

For flag models, hysteresis generally occurs in a transition phase between equilibrium and postequilibrium states, and a bistable state exists within a certain range of the free-stream velocity (Eloy *et al.* 2008; Eloy, Kofman & Schouveiler 2012; Kim *et al.* 2013). Whether gravity and contact affect the emergence of hysteresis in our model is now examined. The width e of hysteresis is defined as $e = (U_{c1,i} - U_{c1,d})/U_{c1,i}$ (Eloy *et al.* 2012). Here $U_{c1,i}$ is the first critical velocity at the transition from the quasistatic equilibrium mode, which is measured while the free-stream velocity increases; and $U_{c1,d}$ is the first critical velocity at the transition to the quasistatic equilibrium mode, and is measured while the free-stream velocity decreases. Hysteresis with a subcritical bifurcation is identified from the plots of normalized amplitude A^* for both profiles of increasing and decreasing free-stream velocities (figure 15*a*); in the figure, $U^*_{c1,i} = 1.27$ and $U^*_{c1,d} = 0.99$. For both the upper and lower walls, the value of e is mostly between 2.6 %–7.8 % (figure 15*b*). Furthermore, to exclude the effect of contact and solely consider the effect of gravity, the case in which contact does not occur is also considered by removing the wall. The value of e averaged over 10 trials is 5.1 % for the non-contact case in the absence of a wall, which is similar to the e values of contact cases. That is, external factors such as gravity and contact do not alter the existence of hysteresis, which is regarded as an inherent characteristic of a fluttering flag.

4. Concluding remarks

We have experimentally investigated the flutter and contact of a horizontal flag near a flat wall under gravitational effects. The flag exhibits diverse dynamic modes according to the flow velocity and the wall distance. For both upper- and lower-wall configurations, the flag undergoes periodic contact with the wall under certain conditions, and the contact

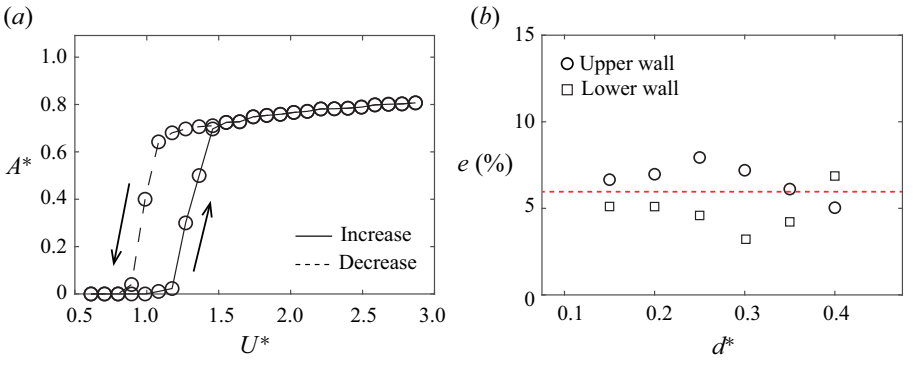

Figure 15. (*a*) Hysteresis of normalized peak-to-peak amplitude A^* for the upper wall: increasing free-stream velocity (solid) and decreasing free-stream velocity (dashed); $[d^*, m^*] = [0.15, 19.16]$. (*b*) Width of hysteresis e for the upper wall (circle) and the lower wall (square); $m^* = 19.16$. The red dashed line denotes the value of e for the case without a wall.

modes can be divided into partial and saturated contact modes based on the contact area and duration. In our flag model, gravity is dominant over the elasticity of the flag, and thus the balance of the fluid inertia and gravitation is considered to characterize the critical conditions and dynamic behaviours of the flag. The relationships between the dimensionless critical flow velocities and the wall distance ratio were examined for the transitions of the dynamic modes using simple scaling analysis. Importantly, the wall distance has a greater influence in determining the critical conditions for the lower wall than for the upper wall. At postequilibrium, the trends of the peak contact force differ depending on the wall location and distance – counter-intuitively, the upper-wall configuration is more beneficial to producing a greater contact force at small wall distances. Due to the conversion to potential energy, the kinetic energy of the flag decreases, having a smaller dimensionless oscillation frequency, compared with typical flag models based on negligible gravity effects.

Although our flag model is limited to two dimensions, the results reported here offer useful information for designing novel energy-harvesting devices based on triboelectric generation. Admittedly, the contact dynamics of the flag, coupled with the free stream, should be analysed in more detail to identify the optimal design of devices in terms of power generation and efficiency. Furthermore, high-fidelity numerical simulations need to be conducted to unravel the evolution of flow structure and the spatial distribution of contact force.

Supplementary movies. Supplementary movies are available at https://doi.org/10.1017/jfm.2023.931

Funding. This research was supported by the Basic Science Research Program through the National Research Foundation of Korea (NRF) funded by the Ministry of Science and ICT (NRF-2020R1A2C2102232) and by the Korea Institute for Advancement of Technology (KIAT) grant funded by the Korea Government (MOTIE) (P0017006, The Competency Development Program for Industry Specialist).

Declaration of interests. The authors report no conflict of interest.

Author ORCIDs.
Minseop Lee https://orcid.org/0009-0005-0441-3392;
Cheolgyun Jung https://orcid.org/0000-0001-6071-9007;
Jeongsu Lee https://orcid.org/0000-0002-7518-7020;
Daegyoum Kim https://orcid.org/0000-0002-7492-4631.

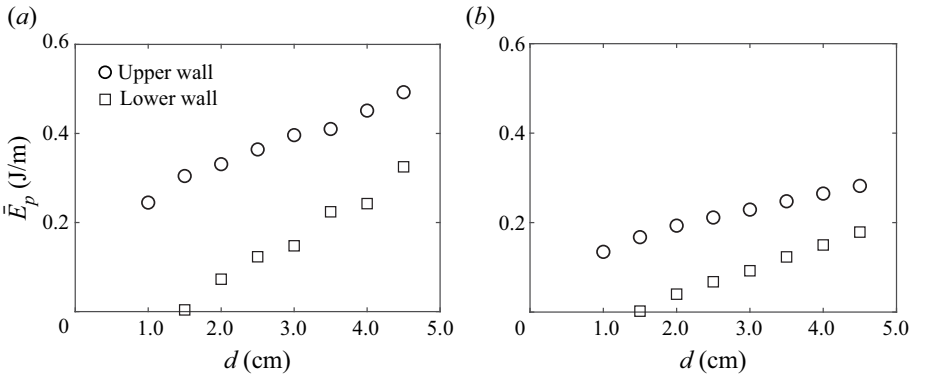

Figure 16. Cycle-averaged potential energy $\bar{E}_p$ versus wall distance d at the second critical velocity for (*a*) $h = 1.0$ mm and (*b*) $h = 0.5$ mm.

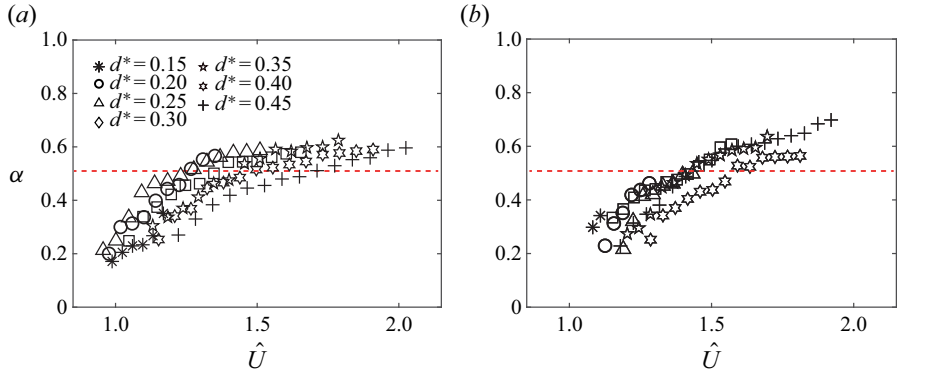

Figure 17. Proportional constant α with respect to dimensionless flow velocity $\hat{U}$ for the lower wall ($d^* = 0.15$–0.45): (*a*) $m^* = 19.16$ and (*b*) $m^* = 9.58$.

Appendix A. Relationship between cycle-averaged potential energy and wall distance

The cycle-averaged potential energy $\bar{E}_p$ of the flag at the second critical velocity U_{c2} for different wall distances d is shown in figure 16. Here $\bar{E}_p$ increases almost linearly with respect to d for both $h = 1.0$ and 0.5 mm. Although the experimental data do not pass through the origin in the figure and the potential energy is a relative quantity depending on a reference height, the change in $\bar{E}_p$ is proportional to the change in d. In this regard, we scale the vertical displacement Δy_G of the centre of the flag as d.

Appendix B. Acquisition of proportional constant α

For the lower wall, we scale the amplitude of the flag A as $d + \alpha l$. For the fitting process, α needs to be determined empirically. From the experimental data, α is obtained under various $\hat{U}$ and d^* conditions in the postequilibrium state, and the averaged value of α is 0.55 for both $m^* = 19.16$ (figure 17*a*) and $m^* = 9.58$ (figure 17*b*). Note that the values of α for the smallest d ($d^* = 0.15$) are much smaller than the average value of 0.55.

References

Akaydin, H.D., Elvin, N. & Andreopoulos, Y. 2010 Wake of a cylinder: a paradigm for energy harvesting with piezoelectric materials. *Exp. Fluids* **49**, 291–304.

Akcabay, D.T. & Young, Y.L. 2012 Hydroelastic response and energy harvesting potential of flexible piezoelectric beams in viscous flow. *Phys. Fluids* **24**, 054106.

Alben, S. 2015 Flag flutter in inviscid channel flow. *Phys. Fluids* **27**, 033603.

Alben, S. & Shelley, M.J. 2008 Flapping states of a flag in an inviscid fluid: bistability and the transition to chaos. *Phys. Rev. Lett.* **100**, 074301.

Allen, J.J. & Smits, A.J. 2001 Energy harvesting EEL. *J. Fluids Struct.* **15**, 629–640.

Argentina, M. & Mahadevan, L. 2005 Fluid-flow-induced flutter of a flag. *Proc. Natl Acad. Sci. USA* **102**, 1829–1834.

Bae, J., Lee, J., Kim, S., Ha, J., Lee, B.S., Park, Y., Choong, C., Kim, J.B., Wang, Z.L. & Kim, H.Y. 2014 Flutter-driven triboelectrification for harvesting wind energy. *Nat. Commun.* **5**, 4929.

Banerjee, S., Connell, B.S.H. & Yue, D.K.P. 2015 Three-dimensional effects on flag flapping dynamics. *J. Fluid Mech.* **783**, 103–136.

Chen, Y., Ryu, J., Liu, Y. & Sung, H.J. 2020 Flapping dynamics of vertically clamped three-dimensional flexible flags in a poiseuille flow. *Phys. Fluids* **32**, 071905.

Connell, B.S.H. & Yue, D.K.P. 2007 Flapping dynamics of a flag in a uniform stream. *J. Fluid Mech.* **581**, 33–67.

Dessi, D. & Mazzocconi, S. 2015 Aeroelastic behavior of a flag in ground effect. *J. Fluids Struct.* **55**, 303–323.

Dunnmon, J.A., Stanton, S.C., Mann, B.P. & Dowell, E.H. 2011 Power extraction from aeroelastic limit cycle oscillations. *J. Fluids Struct.* **27**, 1182–1198.

Ellis, P.D., Williams, J.E. & Shneerson, J.M. 1993 Surgical relief of snoring due to palatal flutter: a preliminary report. *Ann. R. Coll. Surg. Engl.* **75**, 286–290.

Eloy, C., Kofman, N. & Schouveiler, L. 2012 The origin of hysteresis in the flag instability. *J. Fluid Mech.* **691**, 583–593.

Eloy, C., Lagrange, R., Souilliez, C. & Schouveiler, L. 2008 Aeroelastic instability of cantilevered flexible plates in uniform flow. *J. Fluid Mech.* **611**, 97–106.

Fan, F.R., Tian, Z.Q. & Wang, Z.L. 2012 Flexible triboelectric generator. *Nano Energy* **1**, 328–334.

Farnell, D.J., David, T. & Barton, D.C. 2004*a* Numerical simulations of a filament in a flowing soap film. *Intl J. Numer. Meth. Fluids* **44**, 313–330.

Farnell, D.J., David, T. & Barton, D.C. 2004*b* Coupled states of flapping flags. *J. Fluids Struct.* **19**, 29–36.

Giacomello, A. & Porfiri, M. 2011 Underwater energy harvesting from a heavy flag hosting ionic polymer metal composites. *J. Appl. Phys.* **109**, 084903.

Guo, C.Q. & Païdoussis, M.P. 2000 Stability of rectangular plates with free side-edges in two-dimensional inviscid channel flow. *J. Appl. Mech.* **67**, 171–176.

Hœpffner, J. & Naka, Y. 2011 Oblique waves lift the flapping flag. *Phys. Rev. Lett.* **107**, 194502.

Huang, L 1995 Flutter of cantilevered plates in axial flow. *J. Fluids Struct.* **9**, 127–147.

Huang, W.X., Shin, S.J. & Sung, H.J. 2007 Simulation of flexible filaments in a uniform flow by the immersed boundary method. *J. Comput. Phys.* **226**, 2206–2228.

Huang, W.X. & Sung, H.J. 2010 Three-dimensional simulation of a flapping flag in a uniform flow. *J. Fluid Mech.* **653**, 301–336.

Jaiman, R.K., Parmar, M.K. & Gurugubelli, P.S. 2014 Added mass and aeroelastic stability of a flexible plate interacting with mean flow in a confined channel. *J. Appl. Mech.* **81**, 041006.

Jeong, Y.D., Ahn, K.H., Kim, M.J. & Lee, J.H. 2022 Heat transfer enhancement in a channel flow using two wall-mounted flexible flags with a confined cylinder. *Intl J. Heat Mass Transfer* **195**, 123185.

Jia, L.B., Li, F., Yin, X.Z. & Yin, X.Y. 2007 Coupling modes between two flapping filaments. *J. Fluid Mech.* **581**, 199–220.

Jung, C., Song, M. & Kim, D. 2021 Starting jet formation through eversion of elastic sheets. *J. Fluid Mech.* **924**, A7.

Kim, D., Cossé, J., Cerdeira, C.H. & Gharib, M. 2013 Flapping dynamics of an inverted flag. *J. Fluid Mech.* **736**, R1.

Kim, H., Kang, S. & Kim, D. 2017 Dynamics of a flag behind a bluff body. *J. Fluids Struct.* **71**, 1–14.

Kim, H., Lahooti, M., Kim, J. & Kim, D. 2021 Flow-induced periodic snap-through dynamics. *J. Fluid Mech.* **913**, A52.

Kim, S., Huang, W.X. & Sung, H.J. 2010 Constructive and destructive interaction modes between two tandem flexible flags in viscous flow. *J. Fluid Mech.* **661**, 511–521.

KUMAR, D., AREKAR, A.N. & PODDAR, K. 2021 The dynamics of flow-induced flutter of a thin flexible sheet. *Phys. Fluids* **33**, 034131.

LEE, H.J., SHERRIT, S., TOSI, L.P., WALKEMEYER, P. & COLONIUS, T. 2015 Piezoelectric energy harvesting in internal fluid flow. *Sensors* **15**, 26039–26062.

LEE, J., KIM, D. & KIM, H.Y. 2021 Contact behavior of a fluttering flag with an adjacent plate. *Phys. Fluids* **33**, 034105.

LEE, J.B., PARK, S.G., KIM, B., RYU, J. & SUNG, H.J. 2017 Heat transfer enhancement by flexible flags clamped vertically in a Poiseuille channel flow. *Intl J. Heat Mass Transfer* **107**, 391–402.

LEE, S., JOUNG, S. & KIM, D. 2022 Dynamics of a droplet-impact-driven cantilever making contact with the ground. *Phys. Fluids* **34**, 042125.

MICHELIN, S. & DOARÉ, O. 2013 Energy harvesting efficiency of piezoelectric flags in axial flows. *J. Fluid Mech.* **714**, 489–504.

MICHELIN, S., SMITH, S.G.L. & GLOVER, B.J. 2008 Vortex shedding model of a flapping flag. *J. Fluid Mech.* **617**, 1–10.

MOUGEL, J., DOARÉ, O. & MICHELIN, S. 2016 Synchronized flutter of two slender flags. *J. Fluid Mech.* **801**, 652–669.

MOUGEL, J. & MICHELIN, S. 2020 Flutter and resonances of a flag near a free surface. *J. Fluids Struct.* **96**, 103046.

PARK, S.G., KIM, B., CHANG, C.B., RYU, J. & SUNG, H.J. 2016 Enhancement of heat transfer by a self-oscillating inverted flag in a Poiseuille channel flow. *Intl J. Heat Mass Transfer* **96**, 362–370.

QUAN, Z., HAN, C.B., JIANG, T. & WANG, Z.L. 2016 Robust thin films-based triboelectric nanogenerator arrays for harvesting bidirectional wind energy. *Adv. Energy Mater.* **6**, 1501799.

RISTROPH, L. & ZHANG, J. 2008 Anomalous hydrodynamic drafting of interacting flapping flags. *Phys. Rev. Lett.* **101**, 194502.

RYU, J., PARK, S.G., HUANG, W.X. & SUNG, H.J. 2019 Hydrodynamics of a three-dimensional self-propelled flexible plate. *Phys. Fluids* **31**, 021902.

SAWADA, T. & HISADA, T. 2007 Fluid–structure interaction analysis of the two-dimensional flag-in-wind problem by an interface-tracking ALE finite element method. *Comput. Fluids* **36**, 136–146.

SCHOUVEILER, L. & ELOY, C. 2009 Coupled flutter of parallel plates. *Phys. Fluids* **21**, 081703.

SHELLEY, M., VANDENBERGHE, N. & ZHANG, J. 2005 Heavy flags undergo spontaneous oscillations in flowing water. *Phys. Rev. Lett.* **94**, 094302.

SHOELE, K. & MITTAL, R. 2014 Computational study of flow-induced vibration of a reed in a channel and effect on convective heat transfer. *Phys. Fluids* **26**, 127103.

SUN, W., DING, Z., QIN, Z., CHU, F. & HAN, Q. 2020 Wind energy harvesting based on fluttering double-flag type triboelectric nanogenerators. *Nano Energy* **70**, 104526.

TANG, C. & LU, X. 2015 Propulsive performance of two-and three-dimensional flapping flexible plates. *Theor. Appl. Mech. Lett.* **5**, 9–12.

TAYLOR, G.W., BURNS, J.R., KAMMANN, S.A., POWERS, W.B. & WELSH, T.R. 2001 The energy harvesting eel: a small subsurface ocean/river power generator. *IEEE J. Ocean Engng* **26**, 539–547.

TIAN, F.B., LUO, H., ZHU, L. & LU, X.Y. 2011 Coupling modes of three filaments in side-by-side arrangement. *Phys. Fluids* **23**, 111903.

VIROT, E., AMANDOLESE, X. & HÉMON, P. 2013 Fluttering flags: an experimental study of fluid forces. *J. Fluids Struct.* **43**, 385–401.

WANG, L. & TIAN, F.B. 2019 Numerical simulation of flow over a parallel cantilevered flag in the vicinity of a rigid wall. *Phys. Rev.* E **99**, 053111.

WATANABE, Y., SUZUKI, S., SUGIHARA, M. & SUEOKA, Y. 2002 An experimental study of paper flutter. *J. Fluids Struct.* **16**, 529–542.

XU, M., WANG, Y.C., ZHANG, S.L., DING, W., CHENG, J., HE, X., ZHANG, P., WANG, Z., PAN, X. & WANG, Z.L. 2017 An aeroelastic flutter based triboelectric nanogenerator as a self-powered active wind speed sensor in harsh environment. *Extreme Mech. Lett.* **15**, 122–129.

YANG, J., CHEN, Y., ZHANG, J.D., HUANG, W.X. & SUNG, H.J 2021 A self-propelled flexible plate with a keel-like structure. *Phys. Fluids* **33**, 031902.

YU, Z., WANG, Y. & SHAO, X. 2012 Numerical simulations of the flapping of a three-dimensional flexible plate in uniform flow. *J. Sound Vib.* **331**, 4448–4463.

ZHANG, C., HUANG, H. & LU, X.Y. 2020 Effect of trailing-edge shape on the self-propulsive performance of heaving flexible plates. *J. Fluid Mech.* **887**, A7.

ZHANG, J., CHILDRESS, S., LIBCHABER, A. & SHELLEY, M. 2000 Flexible filaments in a flowing soap film as a model for one-dimensional flags in a two-dimensional wind. *Nature* **408**, 835–839.

ZHAO, Z., PU, X., DU, C., LI, L., JIANG, C., HU, W. & WANG, Z.L. 2016 Freestanding flag-type triboelectric nanogenerator for harvesting high-altitude wind energy from arbitrary directions. *ACS Nano* **10**, 1780–1787.

ZHAO, Z., *et al.* 2022 An array of flag-type triboelectric nanogenerators for harvesting wind energy. *Nanomaterials* **12**, 721.

ZHU, L. & PESKIN, C.S. 2003 Interaction of two flapping filaments in a flowing soap film. *Phys. Fluids* **15**, 1954–1960.